IOP Publishing Plasma Physics and Controlled Fusion
Plasma Phys. Control. Fusion **66** (2024) 085004 (9pp) https://doi.org/10.1088/1361-6587/ad15f0

Effects of hydrogen isotope species on ITG microturbulence in LHD

Y Q Qin[1], Y C Chen[1], G Y Sun[1,*], J Nicolau[2] and Z Lin[2]

[1] Department of physics, Xiamen University, Xiamen 361000, People's Republic of China
[2] Department of Physics and Astronomy, University of California, Irvine, CA 92697, United States of America

E-mail: gysun@xmu.edu.cn

Received 3 July 2023, revised 14 November 2023
Accepted for publication 14 December 2023
Published 13 June 2024

Abstract

The linear and nonlinear effects of hydrogen isotope species on ion temperature gradient (ITG) instability in the Large Helical Device (LHD) stellarator are studied using radially global gyrokinetic simulation. We found that the coupling range of linear toroidal harmonics depends on the ion mass of the hydrogen isotope. The growth rates of ITG mode are almost the same for H, D, and T plasmas, indicating a gyro-Bohm scaling of ion-mass dependence. The nonlinear electrostatic simulations show that the zonal flow breaks the radially elongated eigenmode structures and reduces the size of the turbulence eddies, which suppresses the turbulence and the ion heat transport in the LHD. The turbulence amplitude without the zonal flow is almost the same for H, D, and T plasmas, while it decreases with increasing ion mass of the hydrogen isotope when the zonal flow is present. The reduction of the turbulent transport with larger ion mass is mostly due to the enhancement of zonal flows by larger ion mass. The ion heat conductivity deviates from the gyro-Bohm scaling for both cases with and without the zonal flow.

Keywords: stellarator,
ion temperature gradient mode, hydrogen isotope species, radially global gyrokinetic simulation

1. Introduction

One of the most critical issues for the quantitative assessment and forecasting of confinement performance for the burning plasmas is the understanding of micro-instabilities and the resulting turbulent transport of energy and particles (Urano *et al* 2013, Biel *et al* 2019, Yamada *et al* 2019). Since the burning plasma in the stellarator, tokamak, and DEMO reactors are made up of a mixture of hydrogen isotopes like deuterium and tritium, the effects of isotopes on the micro-instabilities, turbulent transport, and zonal flow should be understood in order to achieve improved energy and particle confinements (Osakabe *et al* 2022, Mukhovatov *et al* 2007, Tanaka *et al* 2016).

A large number of studies have shown that the hydrogen isotope ion mass has a significant effect on the energy confinement (Bessenrodt-Weberpals *et al* 1993, Cordey *et al* 1999, Urano *et al* 2013) and fluctuation characteristics (Xu *et al* 2013, Liu *et al* 2015). The isotope ion mass is found to have clear effects on the confinement of trapped electron mode (TEM) in tokamaks, and the temperature profiles can affect the isotope ion effects depending on their gradients (Garcia *et al* 2016). Stellarator is an attractive fusion reactor concept designed with minimal plasma current for the steady-state operation to avoid disruption. In the past two decades, with the improvement of the design and construction of the device, the concept of the stellarator has attracted more attention, and several stellarators have been designed and built. In particular, deuterium experiments have been carried out on the Large Helical Device (LHD) since March 2017, and numerous research have been done on the impact of isotopes on transport (Osakabe *et al* 2018, Takahashi *et al* 2018, Takeiri 2018). Nakata *et al* (2016) found that the linear growth rate of ion temperature gradient (ITG) mode obeys gyro-Bohm ion-mass scaling for ion mass dependence by using Gyrokinetic Vlasov code in flux-tube simulations. Nakata *et al* (2017) found that the combined effects of collisional TEM stabilization by the

* Author to whom any correspondence should be addressed.

isotope ions and the associated increase in the impacts of the steady zonal flows at the near-marginal linear stability lead to a significant transport reduction. Nakata *et al* (2018) studied the transport and confinement characteristics for high T_i/T_e and high T_e/T_i isotope plasmas, and found a significant deviation from the gyro-Bohm scaling for the ion thermal diffusivity. The comparison of transport characteristics between hydrogen and deuterium plasmas in the core region of high-T_i helical plasmas was investigated in Nagaoka *et al* (2019) and found that compared with hydrogen plasma, the ion and electron heat diffusivities in deuterium plasma are lower, which indicates a significant isotope effect.

The isotope effect on the plasma transport is one of the main issues for the LHD and other non-axisymmetric devices, and a complete understanding of the effect of the isotope for microturbulence remains elusive. Hence, the present investigation of the hydrogen isotope effects on ITG turbulence in the LHD contributes to improving the understanding of the isotope effect on microturbulence. Furthermore, the self-generated zonal flow which plays an important role for ITG nonlinear saturation behavior is also considered in our simulations. Finally, although valuable progress has been made for the investigation of microturbulence in stellarators via flux-tube simulations, the radially global simulation is still required because flux-tube simulation results depend on the particular fieldline being simulated and the local assumption is invalid due to the secular radial drift of helically trapped particles across flux surfaces. Nonlinear global gyrokinetic simulations of microturbulence using gyrokinetic toroidal code (GTC) in the tokamaks and stellarators have been extensively verified (Wang *et al* 2020, Tajinder *et al* 2023). In this paper, we use global gyrokinetic simulation to study the hydrogen isotope effects on ITG turbulence in the LHD. We found that the range of coupled ITG modes depends on the ion mass of the hydrogen isotope. The growth rates of ITG mode are almost the same for H, D, and T plasmas, indicating a gyro-Bohm scaling of ion-mass dependence, i.e. $\gamma/k_\perp^2 \propto m_i^{1/2}$. The reduction of the turbulent transport with larger ion mass is mostly due to the enhancement of zonal flows by larger ion mass. The ion heat conductivity deviates from the gyro-Bohm scaling for both cases with and without the zonal flow.

This paper is organized as follows. In section 2 the three-dimensional geometry and global GTC gyrokinetic simulation models for the LHD stellarators are introduced. In section 3, we discuss linear simulation results of the effect of hydrogen isotope on ITG mode in the LHD. Nonlinear simulation results of the effect of hydrogen isotope on ITG mode in the LHD are presented in section 4. Finally, brief conclusions are given in section 5.

2. Simulation models and LHD stellarator

2.1. Simulation models

We start with the gyrokinetic equation describing toroidal plasmas in the five-dimension phase space (Lee 1987, Brizard and Hahm 2007):

$$\frac{\mathrm{d}}{\mathrm{d}t}f(\boldsymbol{X},\mu,v_{||},t)=\left[\frac{\partial}{\partial t}+\dot{\boldsymbol{X}}\cdot\nabla+\dot{v_{||}}\frac{\partial}{\partial v_{||}}\right]f=0, \tag{1}$$

where

$$\dot{\boldsymbol{X}}=v_{||}\boldsymbol{b}+\boldsymbol{v_E}+\boldsymbol{v_d}, \tag{2}$$

and

$$\dot{v_{||}}=-\frac{1}{m}\frac{\boldsymbol{B}^*}{B}\cdot(\mu\nabla B+Z\nabla\phi). \tag{3}$$

Here, we have neglected the collision term for simplicity. f is the particle distribution function, and $\boldsymbol{X}$, μ, $v_{||}$, and t represent the particle guiding center position, the magnetic moment, the parallel velocity, and time, respectively. m is the ion mass, and Z is the ion charge. $\boldsymbol{v_E}$ and $\boldsymbol{v_d}$ are the $\boldsymbol{E}\times\boldsymbol{B}$ drift velocity and magnetic drift velocity, respectively. B is the equilibrium magnetic field, $\boldsymbol{B}^*=\boldsymbol{B}+\frac{Bv_{||}}{\Omega}\nabla\times\boldsymbol{b}$, and $\boldsymbol{b}=\frac{\boldsymbol{B}}{B}$, $\Omega=\frac{Z_\alpha eB}{cm_\alpha}$ is the cyclotron frequency. In this paper, we assume that the electronic response is adiabatic, and we use the electrostatic gyrokinetic equation for ions.We retain the zonal flow generated by ITG turbulence and ignore the equilibrium radial electric field associated with the neoclassical ambipolar electric field in the non-axisymmetrical system for LHD.

The particle-in-cell (PIC) method is used to solve the gyrokinetic equation in the gyrokinetic particle simulation. In order to reduce the Monte-Carlo noise by the PIC method, we used the perturbative δf method (Parker and Lee 1993) for the ion species. We define the ion gyrocenter distribution function $f=f_0+\delta f$, where f_0 and δf are the equilibrium and perturbed distribution functions, respectively. Equation (1) can be expressed as $Lf=0$, where the propagator L is also separated into the equilibrium part L_0 and the perturbed part δL. The equation (1) can be written as

$$(L_0+\delta L)(f_0+\delta f)=0, \tag{4}$$

in which

$$L_0=\frac{\partial}{\partial t}+(v_{||}\boldsymbol{b}+\boldsymbol{v_d})\cdot\nabla-\frac{1}{m}\frac{\boldsymbol{B^*}}{B}\cdot(\mu\nabla B)\frac{\partial}{\partial v_{||}}, \tag{5}$$

$$\delta L=\boldsymbol{v_E}\cdot\nabla-\frac{1}{m}\frac{\boldsymbol{B^*}}{B}\cdot Z\nabla\phi\frac{\partial}{\partial v_{||}}. \tag{6}$$

The equilibrium distribution function f_0 satisfies $L_0f_0=0$, with f_0 is the neoclassical solution. The perturbed distribution function can be calculated as $(L_0+\delta L)\delta f=-\delta Lf_0$. By defining the particle weight as $w=\delta f/f$, we obtain the weight evolution equation,

$$\frac{\mathrm{d}}{\mathrm{d}t}w=(1-w)\left[-\boldsymbol{v_E}\cdot\frac{\nabla f_0}{f_0}+\frac{Z}{mf_0}\frac{\boldsymbol{B^*}}{B}\cdot\nabla\phi\frac{\partial f_0}{\partial v_{||}}\right]. \tag{7}$$

It is noted that we choose a local Maxwell distribution for f_0 and solve equation (7) numerically.

By integrating the perturbed particle distribution, we can obtain the perturbed particle density $\delta n_\alpha=\frac{\pi B_0}{m}\int\delta f_\alpha\mathrm{d}v_{||}\mathrm{d}\mu$,

and consequently, the perturbed electrostatic potential can be calculated by the Poisson equation (Lee 1987)

$$\frac{4\pi Z_i^2 n_i}{T_i}\left(\phi-\tilde{\phi}\right)=4\pi\sum Z_\alpha \delta n_\alpha, \tag{8}$$

The α denotes particle species, and $\tilde{\phi}$ is the secondary gyro-averaged potential,

$$\tilde{\phi}=\int \frac{\mathrm{d}Z(\boldsymbol{X}-\boldsymbol{x}+\boldsymbol{\rho})\overline{\phi}(\boldsymbol{X},\rho)f_{0s}(Z)}{n_{0s}}, \tag{9}$$

where

$$\overline{\phi}(\boldsymbol{X},\boldsymbol{\rho})=1/2\pi\int \mathrm{d}\alpha\mathrm{d}\boldsymbol{X}\delta(\boldsymbol{X}-\boldsymbol{x}+\boldsymbol{\rho})\phi(\boldsymbol{x}), \tag{10}$$

Here, $\overline{\phi}$ is the gyro-averaged potential, and $\boldsymbol{\rho}\equiv-\upsilon_\perp\times\boldsymbol{b_0}/\Omega$ is ion gyro-radius vector.

The motion equation of the guiding center in magnetic coordinates is given by White and Chance (1984), Holod *et al* (2009),

$$\dot{\psi}=\frac{c}{Z}\frac{\partial\epsilon}{\partial B}\left(\frac{I}{D}\frac{\partial B}{\partial\zeta}-\frac{g}{D}\frac{\partial B}{\partial\theta}\right)+\frac{cI}{D}\frac{\partial\phi}{\partial\zeta}-\frac{cg}{D}\frac{\partial\phi}{\partial\theta}, \tag{11}$$

$$\dot{\theta}=\frac{\upsilon_{||}B(1-\rho_c g')}{D}+c\frac{g}{D}\left[\frac{1}{Z}\frac{\partial\epsilon}{\partial B}\frac{\partial B}{\partial\psi}+\frac{\partial\phi}{\partial\psi}\right], \tag{12}$$

$$\dot{\zeta}=\frac{\upsilon_{||}B(q+\rho_c I')}{D}-c\frac{I}{D}\left[\frac{1}{Z}\frac{\partial\epsilon}{\partial B}\frac{\partial B}{\partial\psi}+\frac{\partial\phi}{\partial\psi}\right], \tag{13}$$

$$\begin{aligned}\dot{\rho_{||}}=&-\frac{(1-\rho_c g')}{D}\left[\frac{1}{Z}\frac{\partial\epsilon}{\partial B}\frac{\partial B}{\partial\theta}+\frac{\partial\phi}{\partial\theta}\right]\\&-\frac{(q+\rho_c I')}{D}\left[\frac{1}{Z}\frac{\partial\epsilon}{\partial B}\frac{\partial B}{\partial\zeta}+\frac{\partial\phi}{\partial\zeta}\right],\end{aligned} \tag{14}$$

in which

$$D=gq+I+\rho_c(gI'-Ig') \tag{15}$$

where $I'\equiv\frac{\mathrm{d}I}{\mathrm{d}\psi}$ and $g'\equiv\frac{\mathrm{d}g}{\mathrm{d}\psi}$ are radial derivatives of poloidal and toroidal currents, respectively, and $\rho_c\approx\rho_{||}$ with $\rho_{||}=\frac{\upsilon_{||}}{\Omega}=\frac{mc}{ZB}\upsilon_{||}$, $\frac{\partial\epsilon}{\partial B}=\mu+\frac{Z^2}{mc^2}\rho_{||}^2 B$ (Wang *et al* 2020). It is noted that the nonlinear terms in $\tilde{\phi}$ are only used in later nonlinear simulations.

2.2. LHD stellarator geometry and simulation setup

The GTC is a global three-dimensional code used in the study of microturbulent transport, Alfvén waves, and other physical quantities in toroidal constrained plasmas (Lin *et al* 1998, Xiao *et al* 2015). In the current ITG turbulence simulation, the ideal MHD code VMEC is used to construct the non-axisymmetric equilibrium of the LHD stellarator, which assumes closed magnetic surfaces (Hirshman and Whitson 1983, Lao *et al* 1985, Ferraro and Jardin 2009, Galeotti *et al* 2011, Spong *et al* 2017). VMEC equilibrium data (magnetic field, metric tensor, etc) can be obtained from the poloidal and toroidal Fourier series on a discrete radial mesh (Wang *et al* 2020),

$$B(\psi,\theta,\zeta)=\sum_n\left[B_c(\psi,\theta,n)\cos(n\zeta)+B_s(\psi,\theta,n)\sin(n\zeta)\right] \tag{16}$$

where n is the wave number of toroidal harmonic, B_c, B_s are the Fourier series, (ψ,θ,ζ) are the poloidal flux, poloidal angle, and toroidal angle, respectively, which form the right-handed Boozer coordinates (Boozer 1981). The equilibrium geometry in the Boozer coordinates (ψ,θ,ζ) can be converted to cylindrical coordinates (R,ϕ,Z). Here, ϕ is the toroidal angle in cylindrical coordinates, R and Z are Cartesian coordinates on the poloidal plane (Wang *et al* 2020).

Since the magnetic field period of the LHD stellarator symmetry is $N_{fp}=10$, i.e. there exist ten linear eigenmode families. Each of the ith eigenmode family has multiple eigenstates and consists of coupled toroidal harmonics $n=i+10k$, where k is a positive integer and $i=0,1,2,\ldots,9$. All equilibrium quantities are periodic in the toroidal direction with a period of $2\pi/10$. As a result, we can construct an equilibrium mesh with the toroidal periodicity in the domain $\zeta=[0,2\pi/10]$. The first eigenmode family ($i=0$) can be simulated in one field period of the toroidal domain by using a partial torus geometry, and other eigenmodes exhibit similar results as the first eigenmode family. More toroidal grid points in the equilibrium mesh are used than the parallel grid points in the turbulence mesh for stellarator simulations. We use N_p turbulence mesh in the parallel direction, on which charge density is gathered from particles and Poisson equation is solved, and use N_e extra grid points between every two turbulence grid points, on which equilibrium magnetic fields are calculated and used to push particles. Therefore, the total equilibrium grid points in the toroidal direction are $N_\mathrm{p}(N_\mathrm{e}+1)$. Based on the numerical convergence test, the growth rate and frequencies from simulations show it is sufficient for convergence with the turbulence grid number $N_\mathrm{p}=9$ and the equilibrium grid number $N_\mathrm{e}=2$, respectively. The experimental data for the shot number #146695 at $t=4.300$ s in LHD used in our simulation were given by the LHD team (Fujiwara *et al* 2020). The profile of this shot has been chosen because the ITG turbulence is excited in the presence of both the hydrogen and deuterium so that it is more suitable to study the isotope effects. In addition, this shot has been also used for experimental investigation (Fujiwara *et al* 2020), which will be helpful to compare simulation with experiment in the future. The radial profiles of equilibrium density n, ion temperature T_i, electron temperature T_e, and rotation transform $\iota=1/q$ are shown in figure 1, with q is the safety factor used to describe the magnetic field pitch in the stellarators. In the LHD, for any toroidal angle, the magnetic axis is always located in the same position on the poloidal plane, so R_0 is constant. In our simulations, the major radius $R_0=3.6$ m corresponds to the inward-shifted magnetic configuration. The simulation domain is between $\psi_\mathrm{inner}=0.4\psi_w$ and $\psi_\mathrm{outer}=0.8\psi_w$, and on the diagnostic surface, $r=0.824a$, $\iota=1.04$, $T_e=1.81$ keV, $T_i=1.04$ keV, $T_e/T_i=1.74$,

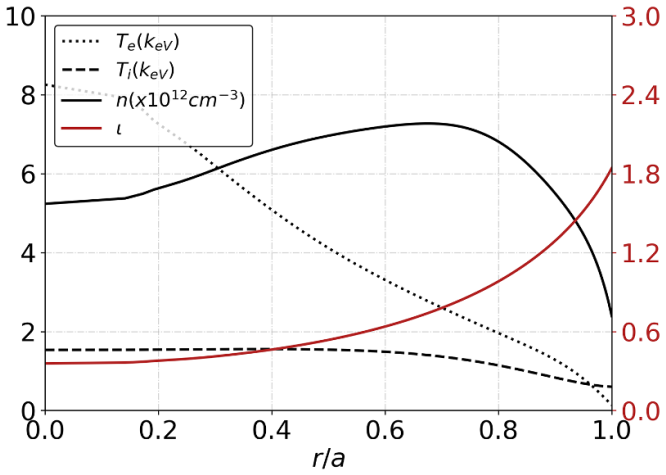

Figure 1. Radial profiles of equilibrium density, temperatures, and rotation transform ι for the shot number #146695 at $t = 4.300$ s in LHD (Fujiwara *et al* 2020).

$n = 6.5810 \times 10^{12}\,\mathrm{cm}^{-3}$, $R_0/L_{T_i} = 15$, $R_0/L_{T_e} = 19$, $R_0/L_n = 9.2$, where $L_T^{-1} = -\mathrm{dln}T/\mathrm{d}r$ and $L_n^{-1} = -\mathrm{dln}n/\mathrm{d}r$ are the characteristic lengths of temperature and density, respectively. In this simulation, the time step size is $\Delta t_\alpha = 0.04R_0/C_{s\alpha}$, where $C_{s\alpha} = \sqrt{T_e/m_{i\alpha}}$ is ion sound speed with $\alpha = \{\mathrm{H}, \mathrm{D}, \mathrm{T}\}$. 110 radial grid points and 2700 poloidal grid points are used for this simulation. It is noted that the particle is returned to the simulation domain and its weight is set to zero when it leaves the radial boundaries of the simulation domain. Because the overall number of markers is maintained constant, particles that leave the radial simulation domain have no effect on the self-consistent electrostatic potential. For simplicity, the effects of fast ion pressure and background shear rotation are ignored.

3. Linear simulation of ITG instability in LHD

The stellarator is non-axisymmetric and has a 3D magnetic geometry, more toroidal grids need to be used in the equilibrium mesh, which will lead to a large number of the parallel wave vector, resulting in a numerical noise problem (Lin *et al* 2002, Wang *et al* 2020). In order to solve this problem, GTC distinguishes the equilibrium mesh from the turbulence mesh in the simulation of the stellarator and uses more toroidal grid points in the equilibrium mesh and less parallel grid points in the turbulence mesh. The numerical convergence test is carried out for the number of parallel grid points (N_p) in turbulent mesh and the number of toroidal grid points (N_e) in equilibrium mesh. The convergence for ITG growth rate and frequency have been tested by varying the equilibrium mesh number N_e and N_p, and it is found that $N_\mathrm{e} = 2$, $N_\mathrm{p} = 9$ is sufficient for convergence in this simulation.

The ITG eigenmode structure on the flux surface (α, ζ) is shown in figure 2, where $\alpha = \theta - \zeta/q$ and ζ are directions perpendicular and parallel to the magnetic field line, respectively. The mode structure on the poloidal plane at $\zeta = 0$ is shown in figure 3, where the color bar represents the amplitude of perturbed electrostatic potential $\delta\phi$. From figure 2, we can see that the ITG eigenmode structure of hydrogen isotope plasmas is narrow in the direction perpendicular to the magnetic field line, but extends in the direction parallel to the magnetic field. In addition, it can be seen from figures 2 and 3 that the width of the filament of ITG eigenmode structure is clearly related to the hydrogen isotope ion mass, that is, the heavier the hydrogen isotope ion mass, the wider the ITG mode filament, which is attributed to the fact that the poloidal wave length of ITG mode increases with decreasing of the ion mass.

The mode structure in figures 2 and 3 is superposition of many harmonics in toroidal direction (figure 2) and poloidal direction (figure 3), which is different from tokamak cases. In order to more accurately analyze the effects of hydrogen isotope on ITG mode toroidal and poloidal eigen harmonics in the LHD, a two-dimensional Fourier transform was performed on the ITG eigenmode structure on the diagnostic magnetic surface in figure 2. The transformation equation is as follows (Wang *et al* 2020)

$$\delta\phi(\psi_d, \theta, \zeta) = \sum_{n,m} \delta\phi_{mn}(\psi_d)\, e^{i(m\theta - n\zeta)}. \tag{17}$$

The 2D contour plot and spectrums on the diagnostic magnetic surface related to the toroidal and poloidal harmonics can be obtained.

The 2D contour plot of $|\delta\phi_{mn}|$ of the ITG eigenmode on the diagnosed flux surface is shown in the figures 4(a)–(c), and the toroidal spectrum of $|\delta\phi_n|$ is given in figures 4(d)–(f), respectively. We can find from upper panels that the ratio of n (the dominant toroidal harmonic) and m (the dominant poloidal harmonic) is approximately equal to the rotational transform $\iota = 1.04$, which is consistent with the theoretical analysis. Besides, it is found that the range of coupled ITG mode depends on the ion mass of hydrogen isotope, the coupled unstable harmonics for H plasma is from $n = 50$ to $n = 130$, while that for D and T plasmas are $[30, 100]$ and $[30, 70]$, respectively, which is consistent with figures 2 and 3. In addition, we found that the maximal growth rate of ITG mode is $0.142C_s/R_0$ for each isotopes' plasma, indicating a gyro-Bohm like ion-mass dependence, i.e. $\gamma/k_\perp^2 \propto m_i^{1/2}$, which is consistent with the result of Nakata *et al* (2016).

4. Nonlinear simulations of ITG turbulence in LHD

In the nonlinear simulations, we use the same magnetic configuration and equilibrium profiles as in the linear simulation, with nonlinear terms in the guiding center motion (those terms are associated with ϕ in equations (11)–(14). Similar with linear simulations, the studies of numerical convergence for the parallel grid number of the turbulence mesh and the toroidal grid number of the equilibrium mesh, as well as time step size, are also carried out in nonlinear simulations. Results show the same grid points and time step size as in the linear simulations are enough for convergence. Therefore, the time step and the

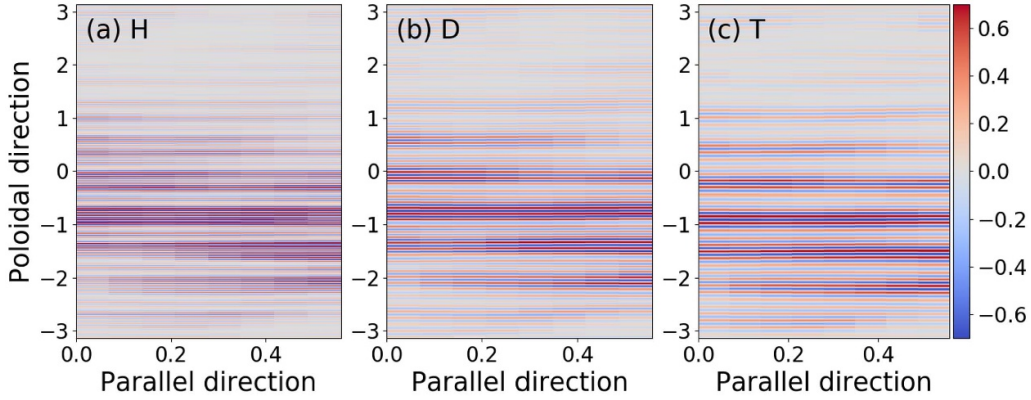

Figure 2. Contour plot of electrostatic potential $\delta\phi$ (arbitrary unit) on the flux surface (α, ζ) of ITG eigenmode, for the H ((a) panel), D ((b) panel) and T ((c) panel) plasmas in the LHD, respectively.

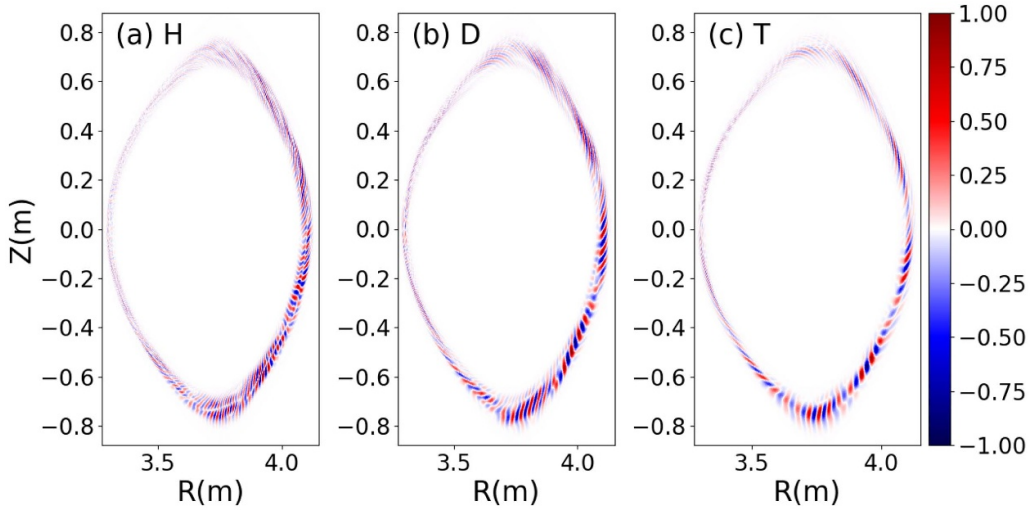

Figure 3. Contour plot of electrostatic potential $\delta\phi$ (arbitrary unit) on the $\zeta = 0$ poloidal plane of ITG eigenmode, for the H ((a) panel), D ((b) panel) and T ((c) panel) plasmas in the LHD, respectively.

grid points are the same as the linear simulation, but the number of particles per cell is increased to reduce the influence of particle noise on the simulation results in the nonlinear simulation. The numerical convergence analysis is shown in figure 5, from which it can be seen that 200 particles in each cell is enough to meet the convergence requirement.

Figure 6 displays the non-zonal electrostatic potentials $\delta\phi$ of ITG mode on the poloidal plane, with and without zonal flow, for H, D, and T plasmas, respectively. It is noted that the electrostatic potential ϕ is decomposed into an averaged zonal component $\langle\phi\rangle$ and a non-zonal component as $\delta\phi = \phi - \langle\phi\rangle$, where the angle bracket $\langle\ldots\rangle$ represents the flux-surface averaging. By comparing figure 6 with figure 3, it can be seen that in the case of H, D, and T plasmas, the radial width of the ITG fluctuation intensity is significantly broadened from the linear to the nonlinear phase, regardless of the zonal flow present or not. As it is known that the saturation intensity of the non-zonal electrostatic potential is suppressed by the zonal flow, we also found that it is stronger in the absence of the zonal flow comparing the case with the zonal flow. Meanwhile, the zonal flow breaks the radially elongated eigenmode structures and reduces the size of the turbulence eddy. We can find that the saturation intensity of the non-zonal electrostatic potential is almost the same for H, D, and T plasmas when the zonal flow is suppressed, see the color bar in figures 6(a), (c) and (e). However, when the zonal flow is added, the saturation intensity of the non-zonal electrostatic potential is quite different for H, D, and T plasmas, that is, the heavier the ion mass of hydrogen isotope, the smaller the intensity of non-zonal electrostatic potential, see the color bar in figures 6(b), (d) and (f). This indicates that the heavier the ion mass, the stronger the suppression effects of the zonal flow on the ITG turbulence in LHD.

The toroidal spectrum of the non-zonal electrostatic potential of the ITG turbulence averaged over the radial domain at $140R_0/C_s$ on the diagnosed flux surface in the nonlinear phase, with and without zonal flow, for H, D, and T plasmas in LHD is shown in figure 7. By comparing figure 7 with figure 4, we

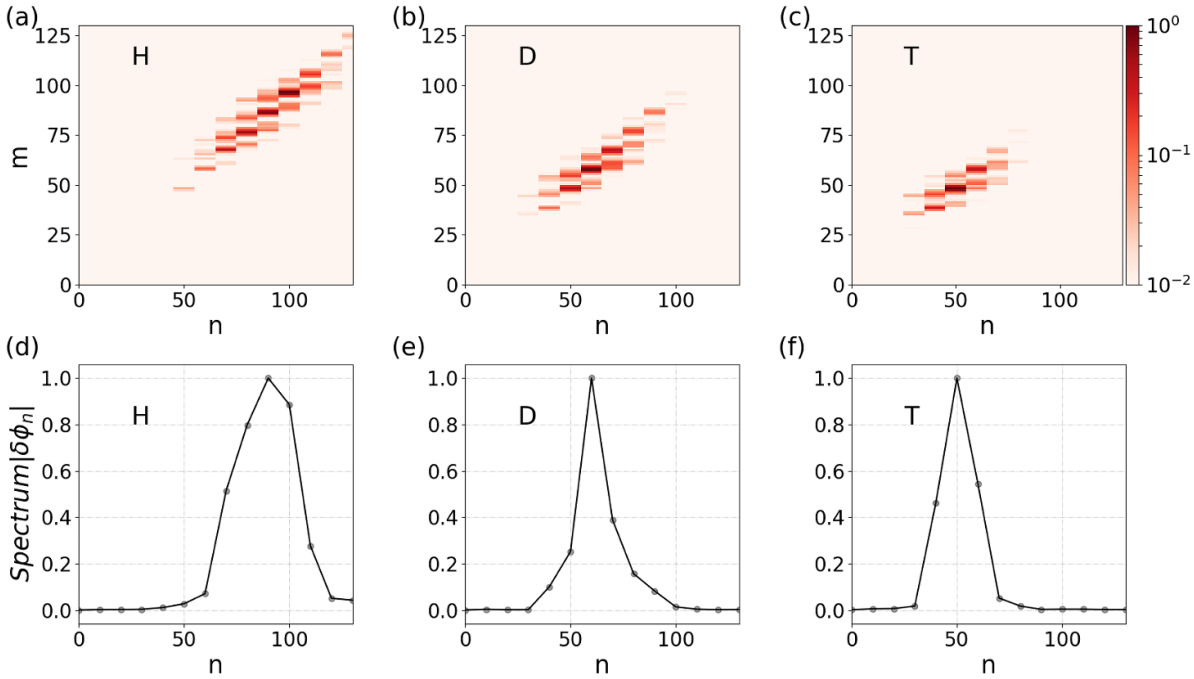

Figure 4. Linear 2D contour plot of $|\delta\phi_{mn}|$ on the diagnosed flux surface $\iota = 1.04$ of ITG eigenmode, for H ((a) panel), D ((b) panel), and T ((c) panel) plasmas in the LHD, respectively. The toroidal spectrum of $|\delta\phi_n|$, for H ((d) panel), D ((e) panel) and T ((f) panel) plasmas, respectively.

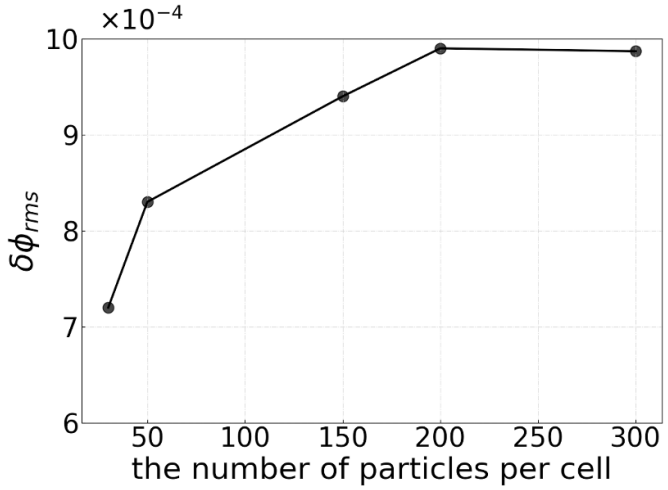

Figure 5. Numerical convergence analysis of the number of particles per cell. Here, the perturbed electrostatic potential is normalized by T_e/e.

can see that the range of unstable n harmonics in all cases of H, D, and T plasmas are significantly wider in the nonlinear phase than that in the linear phase. And the spectrum exhibits an inverse cascade behavior from linear phase to nonlinear phase in all cases of H, D, and T plasmas, i.e. the spectral energy concentration changes from high n and m harmonics in the linear phase to low n and m harmonics in the nonlinear phase. Comparing the upper panels and the lower panels of figure 7, it can be seen that the saturation intensity of electrostatic potential with the zonal flow is smaller than that without zonal flow. We can also find from the upper panels of figure 7 that the intensity of electrostatic potential without the zonal flow is almost the same for H, D, and T plasmas, respectively. However, when the zonal flow is added, we found from the lower panel in figure 7 that the relationship of the maximum value of $\delta\phi_n$ for hydrogen isotope plasma is about $|\delta\phi_n^{\max}|_H = 1.4|\delta\phi_n^{\max}|_D = 2.5|\delta\phi_n^{\max}|_T$, indicating the intensity of electrostatic potential increases with decreasing of the ion mass, which is consistent with the result of figure 6.

The upper panels of figure 8 show the time evolution of the turbulence amplitude $\delta\phi_{\rm rms}$ of the ITG (defined as the root mean square of the non-zonal electrostatic potential), and the volume-averaged ion heat conductivity χ_i, with and without zonal flow, for H, D, and T plasmas, respectively. The lower panels show the time evolution of the zonal electrostatic potential $\phi_{\rm ZF}$, and the ratio of the $\phi_{\rm ZF}$ and $\delta\phi_{\rm rms}$ in the presence of the zonal flow for H, D, and T plasmas, respectively. In this simulation, the electrostatic potentials are normalized by T_e/e, and the heat conductivity χ_i is normalized by $\chi_{\rm GB} = \chi_{\rm B}\rho_{i\alpha}^*$, where $\chi_{\rm B} = cT_e/eB$, and $\rho_{i\alpha}^* = v_i m_{i\alpha} c/eBa$, and $m_{i\alpha}$ is each particle species. We can see that $\delta\phi_{\rm rms}$ (figure 8(a)) and χ_i (figure 8(b)) first increase exponentially in the linear stage and then saturate in the nonlinear stage. When zonal flow is artificially suppressed, the saturation level of $\delta\phi_{\rm rms}$ and χ_i are higher, comparing the case with the zonal flow, which is resulted from the fact that the zonal flow can break the radially elongated eigenmode structures, reduce the size of the turbulence eddy, and suppress turbulent transport in the LHD. Turning to the effects of isotope, we can find that the turbulence amplitude $\delta\phi_{\rm rms}$ is almost the same for the H, D, and T plasmas when the zonal flow is suppressed. However, when the

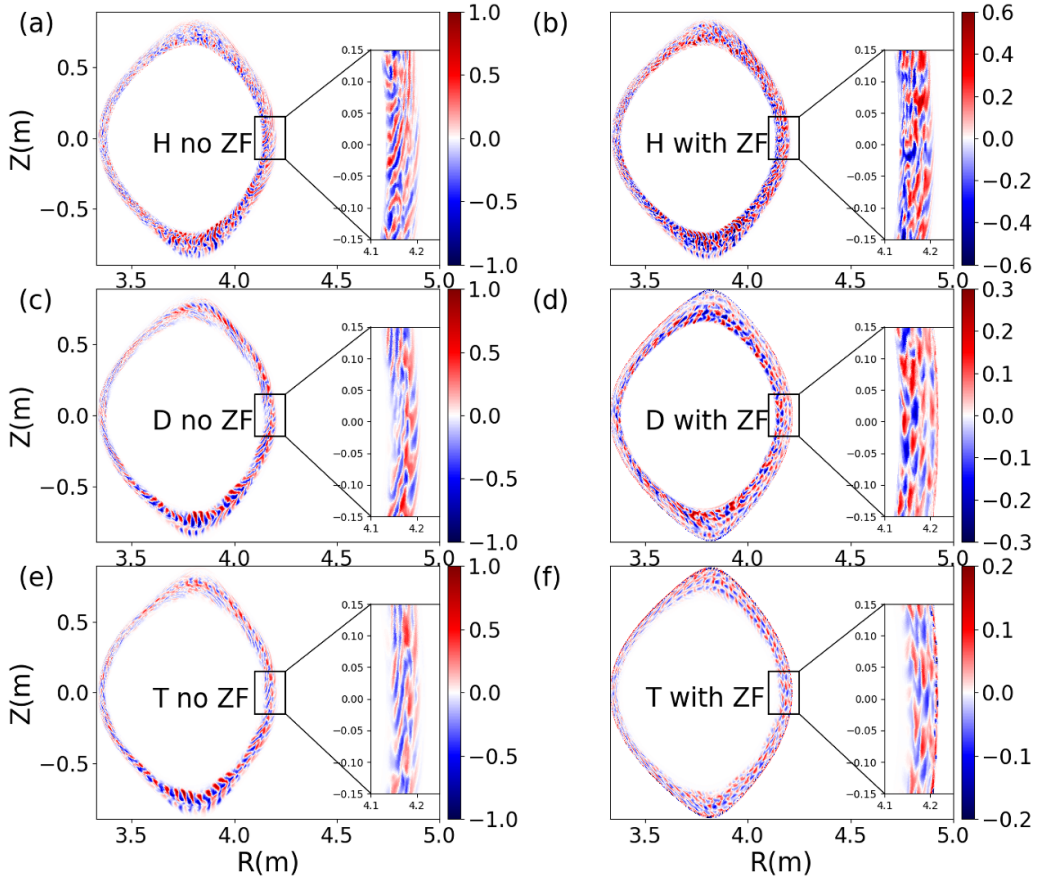

Figure 6. Poloidal contour plot of non-zonal electrostatic potential $\delta\phi$, without and with the zonal flow, for H, D, and T plasmas in the LHD, respectively.

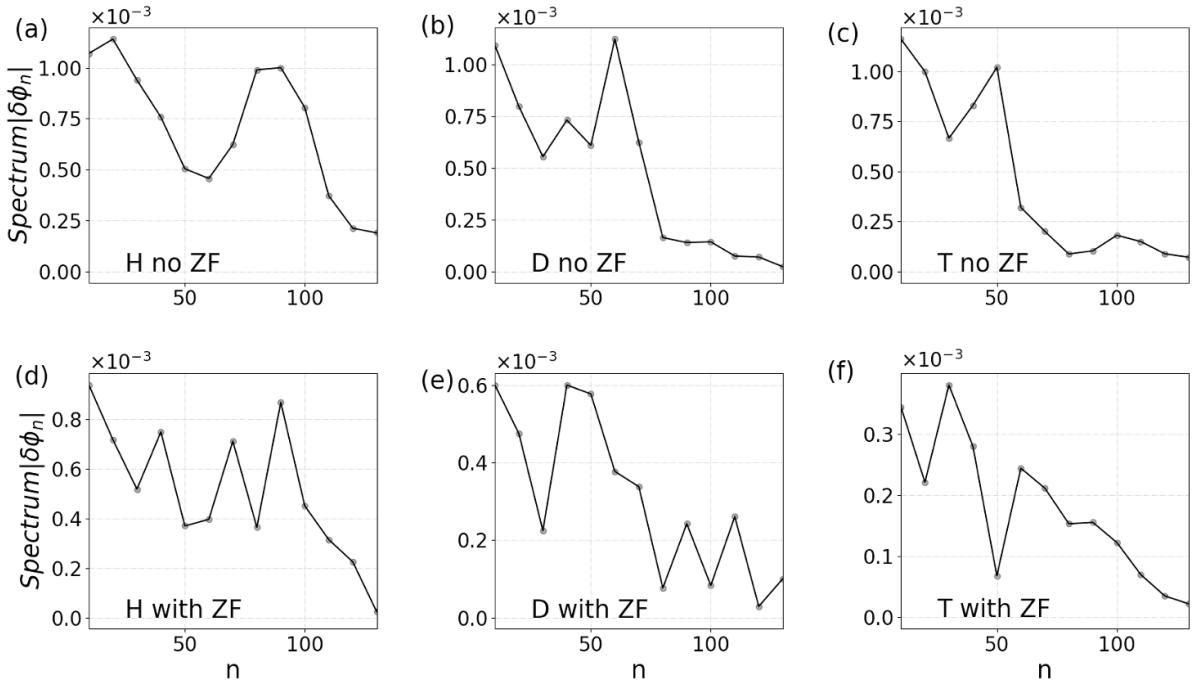

Figure 7. Nonlinear toroidal spectrum $|\delta\phi_{mn}|$ averaged over the radial domain at $140R_0/C_s$ on the diagnosed flux surface of non-zonal electrostatic potential, without and with the zonal flow, for H, D, T plasmas in the LHD, respectively.

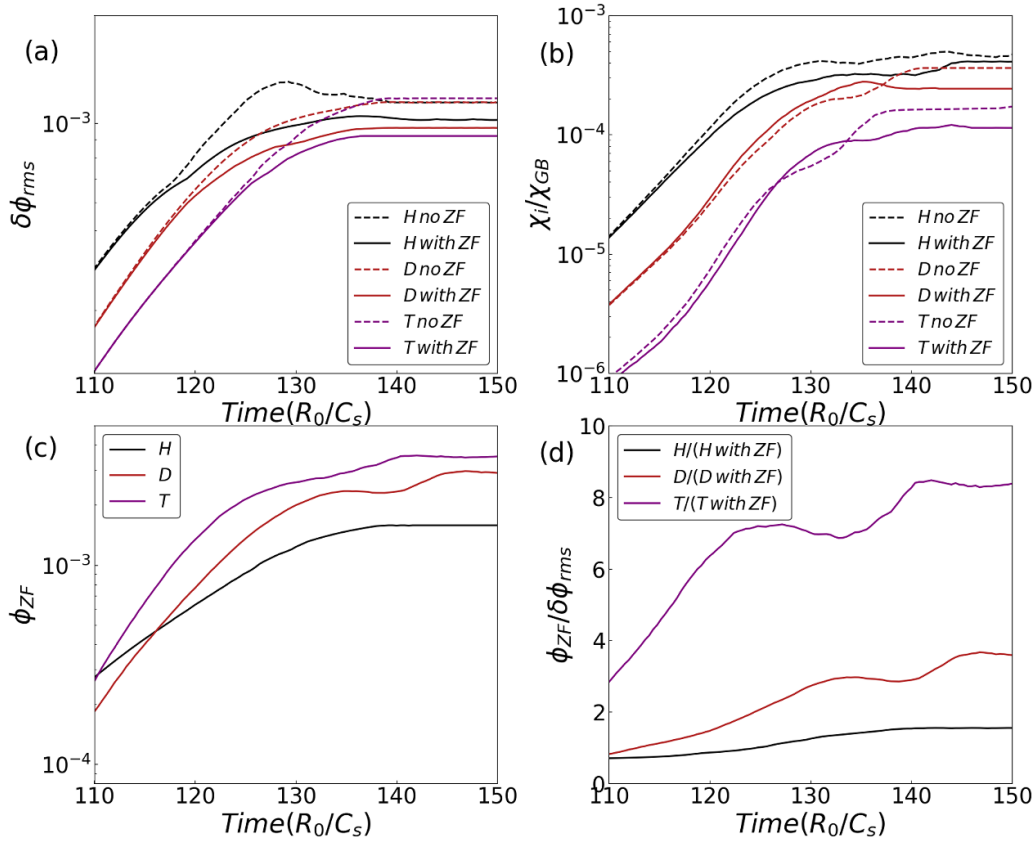

Figure 8. Time evolution of volume averaged the non-zonal electrostatic potential $\delta\phi_{\rm rms}$ ((a) panel), and the ion heat conductivity ((b) panel), and the zonal electrostatic potential $\phi_{\rm ZF}$ (c panel), with and without the zonal flow of the ITG mode, for H, D, and T plasmas in the LHD, respectively. (c) and (d) panels show the time evolution of the zonal electrostatic potential $\phi_{\rm ZF}$, and the ratio of the $\phi_{\rm ZF}$ and $\delta\phi_{\rm rms}$ in the presence of the zonal flow for H, D, and T plasmas, respectively.

zonal flow is considered, the turbulence amplitude decreases with increasing ion mass of the hydrogen isotope. This is consistent with the results in figures 6 and 7. Meanwhile, we found from figure 8(b) that the ion mass dependence of the ion heat conductivity deviates from the gyro-Bohm scaling clearly, that is $(\chi_{i(\rm D)}/\chi_{\rm GB(D)})/(\chi_{i(\rm H)}/\chi_{\rm GB(H)}) = 0.56$, $(\chi_{i(\rm T)}/\chi_{\rm GB(T)})/(\chi_{i(\rm H)}/\chi_{\rm GB(H)}) = 0.27$, we note that $T_e/T_i = 1.74$. It is consistent with the experimental result of Nakata *et al* (2018), which shows that deviation from the gyro-Bohm scaling is $(\chi_{i(\rm D)}/\chi_{\rm GB(D)})/(\chi_{i(\rm H)}/\chi_{\rm GB(H)}) = 0.31$ for the high T_i/T_e and $(\chi_{i(\rm D)}/\chi_{\rm GB(D)})/(\chi_{i(\rm H)}/\chi_{\rm GB(H)}) = 0.37$ for the high T_e/T_i. In addition, we can see that the line shape of the root mean square of the perturbed electrostatic potential and the ion thermal conductivity is quite similar, which indicates that the ion heat transport is driven by the turbulence of the perturbed electrostatic potential, which is consistent with Xiao and Lin (2009). More importantly, lower panels of figure 8 show that intensity of zonal flows increases with larger ion mass, while intensity of the turbulence decreases with larger ion mass. We conclude that the isotope effects on the ITG transport mostly comes from the enhancement of the zonal flows by the larger ion mass, in qualitative agreement with earlier local gyrokinetic stimulation of the TEM turbulence in the LHD stellarator (Nakata *et al* 2017).

5. Conclusions

We have investigated the effects of the hydrogen isotope species on ITG turbulence in LHD using the global gyrokinetic simulation. The linear simulations show that the range of coupled ITG mode depends on the ion mass of the hydrogen isotope, the heavier the ion mass, the more coupling toroidal harmonics. The growth rate profiles of ITG mode are almost the same for H, D, and T plasma, indicating a gyro-Bohm scale ion-mass dependence, i.e. $\gamma/k_\perp^2 \propto m_i^{1/2}$. The nonlinear simulations show that the zonal flow breaks the radially elongated eigenmode structures and reduces the size of the turbulence eddies. The spectrum of the non-zonal modes exhibits an inverse cascade behavior from linear phase to nonlinear phase in all cases of H, D, and T plasmas. The turbulence amplitude $\delta\phi_{\rm rms}$ without zonal flow is almost the same for H, D, and T plasmas, while the turbulence amplitude decreases with increasing the ion mass of the hydrogen isotope when the zonal flow is considered. The reduction of the ion heat conductivity for the larger ion mass is mostly from the enhancement of zonal flows by the larger ion mass. The ion heat conductivity deviates from the gyro-Bohm scaling for both cases with and without the zonal flow, which is consistent with the experimental result of Nakata *et al* (2017).

The simulation will be improved by using kinetic electrons response in the future study. Furthermore, the collisional effects enhancing the zonal flow damping and turbulent transport will be also considered (Lin *et al* 1999). Finally, the mechanism for the enhancement of zonal flows by the larger ion mass will be studied.

Data availability statement

The data supporting the findings of this study are available in the LHD experiment data repository at https://doi.org/10.57451/lhd.analyzed-data.

Acknowledgments

The authors would like to thank the LHD team for the experimental data, and the GTC team for helpful discussions. This work was supported by National Key R&D Program of China under Grant No. 2017YFE0301201 and National Natural Science Foundation of China (NSFC) under Grant No. 11275162, US DOE Award No. DE-FG02-07ER54916, SciDAC and INCITE programs, and the NIFS Collaboration Research program (NIFS22KIST035).

ORCID iDs

Y Q Qin https://orcid.org/0000-0003-4927-1648
Y C Chen https://orcid.org/0000-0001-9054-2791
G Y Sun https://orcid.org/0000-0001-6382-6254
J Nicolau https://orcid.org/0000-0003-1470-1820
Z Lin https://orcid.org/0000-0003-2007-8983

References

Bessenrodt-Weberpals M *et al* 1993 *Nucl. Fusion* **33** 1205
Biel W *et al* 2019 *Fusion Eng. Des.* **146** 465–72
Boozer A H 1981 *Phys. Fluids* **24** 1999–2003
Brizard A J and Hahm T S 2007 *Rev. Mod. Phys.* **79** 421
Cordey J *et al* 1999 *Nucl. Fusion* **39** 301
Ferraro N M and Jardin S C 2009 *J. Comput. Phys.* **228** 7742–70
Fujiwara Y *et al* 2020 *Nucl. Fusion* **60** 112014
Galeotti L, Barnes D, Ceccherini F and Pegoraro F 2011 *Phys. Plasmas* **18** 082509
Garcia J, Görler T, Jenko F and Giruzzi G 2016 *Nucl. Fusion* **57** 014007
Hirshman S P and Whitson J 1983 *Phys. Fluids* **26** 3553–68
Holod I, Zhang W, Xiao Y and Lin Z 2009 *Phys. Plasmas* **16** 122307
Lao L, Greene J, Wang T, Helton F and Zawadzki E 1985 *Phys. Fluids* **28** 869–77
Lee W 1987 *J. Comput. Phys.* **72** 243–69
Lin Z, Ethier S, Hahm T and Tang W 2002 *Phys. Rev. Lett.* **88** 195004
Lin Z, Hahm T S, Lee W W, Tang W M and Diamond P H 1999 *Phys. Rev. Lett.* **83** 3645–8
Lin Z, Hahm T S, Lee W W, Tang W M and White R B 1998 *Science* **281** 1835–7
Liu B *et al* 2015 *Nucl. Fusion* **55** 112002
Mukhovatov V *et al* 2007 *Nucl. Fusion* **47** S404
Nagaoka K *et al* (the LHD Experiment Group) 2019 *Nucl. Fusion* **59** 106002
Nakata M, Nagaoka K, Tanaka K, Takahashi H, Nunami M, Satake S, Yokoyama M and Warmer F (the LHD Experiment Group) 2018 *Plasma Phys. Control. Fusion* **61** 014016
Nakata M, Nunami M, Sugama H and Watanabe T H 2016 *Plasma Phys. Control. Fusion* **58** 074008
Nakata M, Nunami M, Sugama H and Watanabe T H 2017 *Phys. Rev. Lett.* **118** 165002
Osakabe M *et al* 2022 Recent results from deuterium experiments on the large helical device and their contribution to fusion reactor development Nucl. Fusion **62** 042019
Osakabe M, Isobe M, Tanaka M, Motojima G, Tsumori K, Yokoyama M, Morisaki T and Takeiri Y 2018 *IEEE Trans. Plasma Sci.* **46** 2324–31
Parker S and Lee W 1993 *Phys. Fluids* B **5** 77–86
Singh T, Javier H N, Nespoli F, Motojima G, Lin Z, Sen A, Sharma S and Kuley A 2023 *Nucl. Fusion* **64** 016007
Spong D A, Holod I, Todo Y and Osakabe M 2017 *Nucl. Fusion* **57** 086018
Takahashi H *et al* 2018 *Nucl. Fusion* **58** 106028
Takeiri Y 2018 *IEEE Trans. Plasma Sci.* **46** 2348–53
Tanaka K, Okamura S, Minami T, Ida K, Mikkelsen D R, Osakabe M, Yoshimura Y, Isobe M, Morita S and Matsuoka K 2016 *Plasma Phys. Control. Fusion* **58** 055011
Urano H *et al* 2013 *Nucl. Fusion* **53** 083003
Wang H, Holod I, Lin Z, Bao J, Fu J Y, Liu P, Nicolau J H, Spong D and Xiao Y 2020 *Phys. Plasmas* **27** 082305
White R B and Chance M 1984 *Phys. Fluids* **27** 2455–67
Xiao Y, Holod I, Wang Z, Lin Z and Zhang T 2015 *Phys. Plasmas* **22** S18–127
Xiao Y and Lin Z 2009 *Phys. Rev. Lett.* **103** 085004
Xu Y, Hidalgo C, Shesterikov I, Krämer-Flecken A, Zoletnik S, Van Schoor M and Vergote M (the TEXTOR Team) 2013 *Phys. Rev. Lett.* **110** 265005
Yamada H *et al* (LHD Experiment Group) 2019 *Phys. Rev. Lett.* **123** 185001